Scientific Research Publishing

Energy and Power Engineering, 2025, 17(3), 35-54
https://www.scirp.org/journal/epe
ISSN Online: 1947-3818
ISSN Print: 1949-243X

Speed Regulation of a Mill Driven by an Asynchronous Machine Powered by Photovoltaic Solar Energy: Modeling, Control and Optimization

Abdoulaye Kebe, Papa Demba Ba, Ibrahima Gueye, Abdoulaye Sall, Cheikh Sene

Ecole Normale Superieure D'Enseignement Technique Professionnel (ENSETP), Cheikh Anta DIOP University, Dakar, Senegal
Email: abdoulaye.kebe@ucad.edu.sn, bapapademba1997@gmail.com, ibrahima64.gueye@ucad.edu.sn

How to cite this paper: Kebe, A., Ba, P.D., Gueye, I., Sall, A. and Sene, C. (2025) Speed Regulation of a Mill Driven by an Asynchronous Machine Powered by Photovoltaic Solar Energy: Modeling, Control and Optimization. *Energy and Power Engineering*, **17**, 35-54.
https://doi.org/10.4236/epe.2025.173003

Received: February 2, 2025
Accepted: March 28, 2025
Published: March 31, 2025

Copyright © 2025 by author(s) and Scientific Research Publishing Inc.
This work is licensed under the Creative Commons Attribution International License (CC BY 4.0).
http://creativecommons.org/licenses/by/4.0/

Open Access

Abstract

This paper focuses on the speed control of a mill driven by an Asynchronous Motor (AM) powered by a solar photovoltaic energy source. As solar energy gains importance in the energy transition, artisanal mills are showing promise in improving rural life. However, speed variations caused by solar irradiance can affect their efficiency. The study proposes a comprehensive modeling of the system and explores advanced control strategies and optimization methods to optimize the performance. Traditional control approaches based on Foc and scalar strategies are examined, and the optimization considers the control and design parameters of the photovoltaic system. The results obtained by simulations in Simulink confirmed the performance of the strategies with good speed control regardless of the variation of load and irradiation.

Keywords

Photovoltaic Generator, Boost Converter, MPPT, Inverter, Asynchronous Motor, Artisanal Mill

1. Introduction

This paper focuses on the speed control of a mill driven by an Induction Motor (IM) powered by a solar photovoltaic energy source. With the increasing focus on energy transition and the need to develop sustainable energy sources, the use of solar photovoltaic energy to power autonomous and decentralized systems is gaining popularity [1]. Among these emerging applications, small-scale mills driven by Induction Motors (IM) represent a promising solution for cereal processing in remote rural areas, thus offering several opportunities for improving

living conditions and socio-economic development [1] [2]. However, variations in solar irradiance throughout the day and weather conditions can lead to fluctuations in the speed of the motor mechanically coupled to the mill. This can affect the overall efficiency of the system and compromise the reliability of the power supply. Thus, precise motor speed control becomes a crucial challenge to ensure stable and efficient operation. In our paper, we focus on the in-depth study of speed control of a mill driven by a Three-Phase Induction Motor (SAM), powered by solar photovoltaic energy [3]. The main objective of this paper is to present a detailed modeling of the system, design an advanced control strategy and explore optimization techniques to improve the overall system performance [4] [5]. In the following sections, we will discuss the mathematical modeling of the entire system, including the mill, the Three-Phase Induction Motor (SAM) and the photovoltaic system composed of panels, a chopper and an inverter. This will provide a solid theoretical basis for the development of the control [6]. Then, we will examine the different control approaches, namely scalar control and vector control. Subsequently, we will focus on the optimization of the system performance, taking into account the control parameters and the design of the photovoltaic system. The obtained results will be validated through simulations on Matlab-Simulink software. Finally, we will conclude by highlighting the contributions and limitations of this study, while proposing future research avenues to optimize the performance of MAS-driven mills further. Through this work, we hope to make a significant contribution to the understanding and improvement of speed regulation in solar mill systems, thus paving the way for wider applications of this clean and renewable technology in remote regions of the world.

2. System Diagram

Figure 1 below shows the system in its entirety. It consists of a photovoltaic generator, a chopper, a three-phase inverter and a grinding device consisting of a homemade grinder and an induction motor. To simulate the system, it is necessary to model the different parts that compose it.

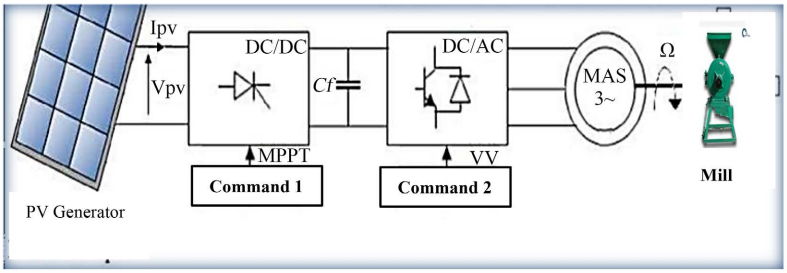

Figure 1. System diagram.

3. Modeling of System Elements

3.1. Modeling of the Photovoltaic Generator

There are different types of solar (photovoltaic) cells, and each type of cell has its

own efficiency and cost [6] [7]. In this article, we study the single-diode model where the cell is presented as an electric current generator whose behavior is equivalent to a current source shunted by a single diode. To take into account physical phenomena at the cell level, the model is completed by a series resistor Rs shunt or parallel resistor Rp. The equivalent electrical diagram of the photovoltaic cell is given in (**Figure 2**) below [7].

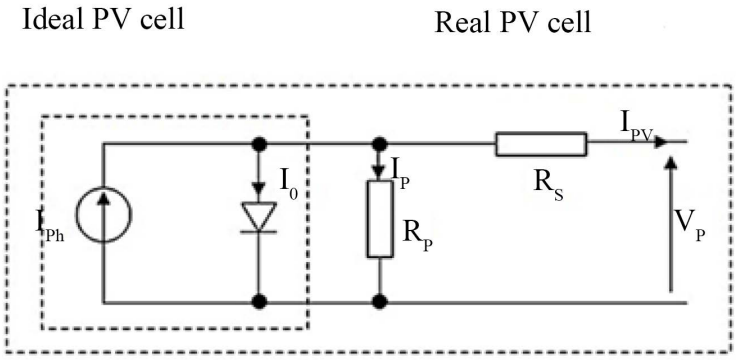

Figure 2. Equivalent model of a photovoltaic cell.

The expression of the current characteristic of the photovoltaic panel (Ipv) is expressed as [7] follows:

$$Ipv = Iph - \mathrm{Is}\left[\exp\left(\frac{q(V+I.Rs)}{K.Tc.A}-1\right)\right]-\frac{V+I.Rs}{Rp} \quad (1)$$

The equation giving the current characteristic of a GPV can be written as follows:

$$I = Np.Iph - Np.Is\left[\exp\left(\frac{qVoc}{Ns.A.K.Tc}\right)-1\right]-\frac{\left(\frac{Np.V}{Np}+I.Rs\right)}{Rp} \quad (2)$$

Technical Characteristics of the Panel

In this article, the work was done with the solar panel of type:

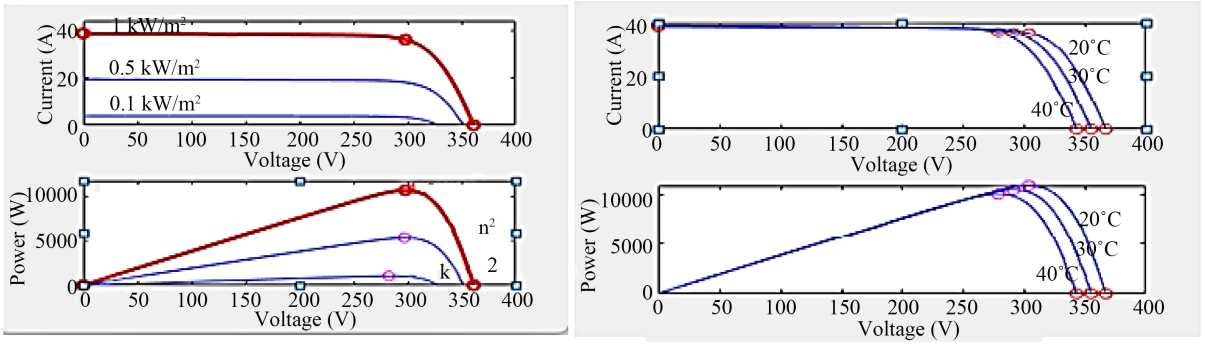

Figure 3. Simulation result of the model under the variation of solar irradiance and the variation of temperature.

SOLTON Power SPI-215P whose electrical characteristics are shown in Figure 3 above.

The following figures represent respectively the current-voltage, power-voltage characteristics for a temperature T = 298 K° and a variable illumination (E) of [1,0.8, 0.6, 0.4, 0.2] * 1000 W/m² and also a variable temperature of [40 30 20]°C.

➢ **Characteristic of I = f (V) and P = f (V)**

3.2. Boost Chopper Modeling

The use of DC-DC converters allows the control of electrical power in circuits operating in direct current with great flexibility and high efficiency which in our case will allow us to pursue the optimum operating point [7] [8]. In our article, we have a Boost type converter whose electrical diagram is given in Figure 4 below.

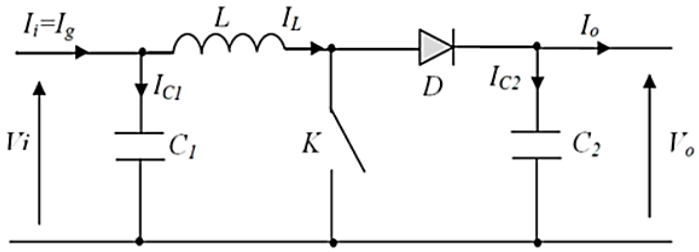

Figure 4. Electrical circuit of a boost chopper.

3.2.1. Mathematical Modeling of the Boost Chopper

The application of Kirchhoff's laws (Knot and Mesh) on the two equivalent circuits of the two operating phases gives [8]:

$$0 < t < DTs$$

$$DTs < t < Ts$$

$$\begin{cases} i_{C1} = C_1 \dfrac{dv_i}{dt} = i_i - i_L \\ i_{C2} = C2 \dfrac{dv_0}{dt} = -i_0 \\ v_L = L \dfrac{di_l}{dt} = v_i - R_L i_L \end{cases} \quad (3)$$

$$\begin{cases} i_{C1} = C_1 \dfrac{dv_i}{dt} = i_i - i_L \\ i_{C2} = C2 \dfrac{dv_0}{dt} = i_L - i_0 \\ v_L = L \dfrac{di_L}{dt} = v_i - v_0 - R_L i_L \end{cases} \quad (4)$$

D: The duty cycle of the pulses that control the switch.

Ts: Being the period of impulses

3.2.2. Approximate Model of the Boost Chopper

By applying to the systems of equations (3) and (4) we can obtain the following

relations [9] [10]:

$$\begin{cases} i_L = i_i - C_1 \dfrac{dv_i}{dt} \\ i_0 = (1-D) i_L - C2 \dfrac{dv_0}{dt} \\ v_i = (1-D) v_0 + R_L i_L + L \dfrac{di_L}{dt} \end{cases} \tag{5}$$

3.2.3. Calculates Chopper Parameters

Output current: $Io = \dfrac{P}{Vo}$

Percentage of voltage variation: $\Delta V = 1\%$

Percentage of current variation: $\Delta I = 5\%$

Inductance: $L = \dfrac{Vin(Vo - Vin)}{\Delta I * fs * Vo} = 1.45mH$

Ability: $C = \dfrac{Io(Vo - Vin)}{fs * \Delta Vo * Vo} = 3227uF$

3.2.4. MPPT Control

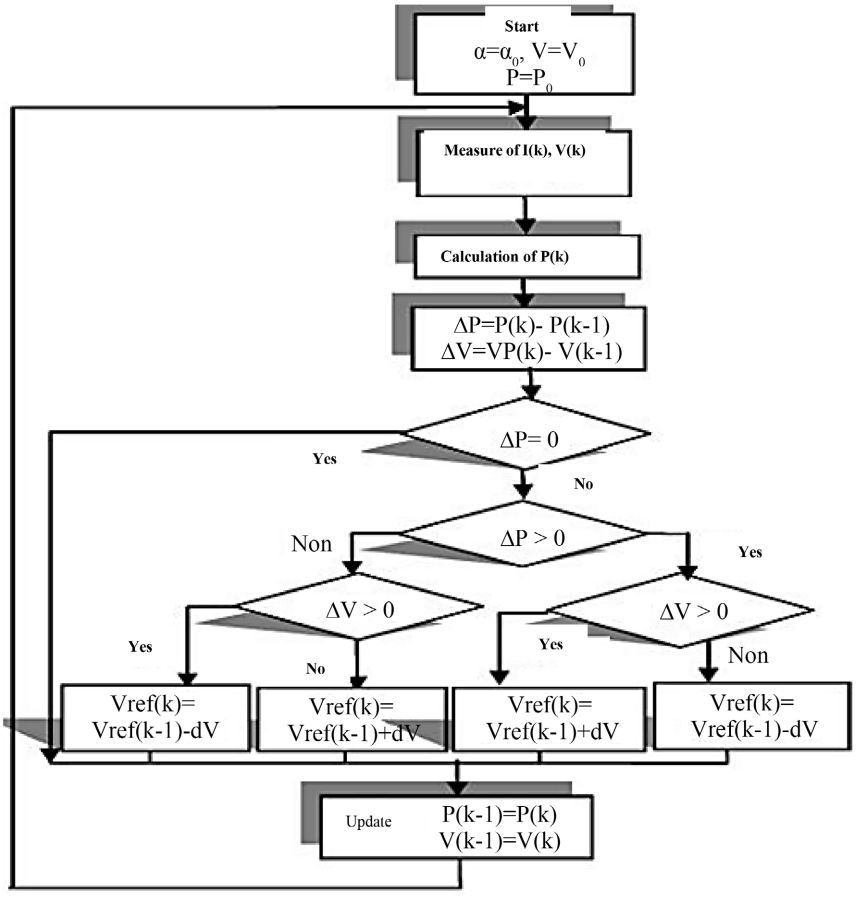

Figure 5. Flowchart of the P&O algorithm.

In this part, we present a P&O control algorithm for tracking the maximum power delivered by the photovoltaic generator [11] [12]. The principle of this algorithm is to perform a disturbance on the voltage of the panel Vpv while acting on the duty cycle α. Indeed, following this disturbance, we calculate the power supplied by the PV panel at time k, then we compare it to the previous one at time (k – 1). If the power increases, we approach the maximum power point, "PMP" and the variation of the duty cycle is maintained in the same direction [13]. On the contrary, if the power decreases, we move away from the maximum power point, "PMP". Then, we must reverse the direction of the variation of the duty cycle [14]. The general algorithm of this control is given by (**Figure 5**) below.

The program corresponding to this algorithm has been implemented in the Matlab/Simulink environment.

3.3. Inverter Modeling

The operation of the inverter is based on the switching state of the switches. Switching is provided by three logic functions (Sa, Sb, Sc) [14] [15]. These functions made it possible to establish the relationship (10) between the voltages in three phases (Va Vb Vc) of the millet mill actuator and the voltage of the direct current source (Vdc).

We can then model the inverter by a matrix $[T]$ ensuring the continuous-alternating transition $[Vac]=[T][Vdc]$ with [15] [16]:

$$\begin{bmatrix} \boldsymbol{Va} \\ \boldsymbol{Vb} \\ \boldsymbol{Vc} \end{bmatrix} = \left[\frac{\mathbf{Vdc}}{3}\right] \begin{bmatrix} 2 & -1 & -1 \\ -1 & 2 & -1 \\ -1 & -1 & 2 \end{bmatrix} \begin{bmatrix} \boldsymbol{Sa} \\ \boldsymbol{Sb} \\ \boldsymbol{Sc} \end{bmatrix} \tag{6}$$

3.4. Modeling of the Grinding Device

The cage asynchronous machine is the most used actuator in most motorized applications due to its simplicity, robustness and cost [17]. To simulate the mill with the machine it is necessary to proceed with its modeling.

3.4.1. Modeling of the Asynchronous Motor in the Three-Phase Plane

The stator of the Asynchronous Machine (MAS) receives its power supply from a balanced three-phase voltage system. This power supply generates the formation of a rotating magnetic field (in accordance with the FERRARIS theorem) inside the space between the stator and the rotor of the machine called the air gap (as illustrated in **Figure 6**) [18] [19].

The voltage equations for the three stator phases and the three rotor phases are as follows [19]-[21]:

$$\begin{cases} Va = VmaxSin(\theta) \\ Vb = VmaxSin\left(\theta - \dfrac{2\pi}{3}\right) \\ Vc = VmaxSin\left(\theta - \dfrac{4\pi}{3}\right) \end{cases} \tag{7}$$

Equation statoriques:

$$\begin{cases} Vsa = Rs * isa + L\dfrac{d}{dt}isa \\ Vsb = Rs * isb + L\dfrac{d}{dt}isb \\ Vsc = Rs * isc + L\dfrac{d}{dt}isc \end{cases} \quad (8)$$

Equations Rotoriques:

$$\begin{cases} Vra = Rr * ira + L\dfrac{d}{dt}ira \\ Vrb = Rr * irb + L\dfrac{d}{dt}irb \\ Vrc = Rr * irc + L\dfrac{d}{dt}irc \end{cases} \quad (9)$$

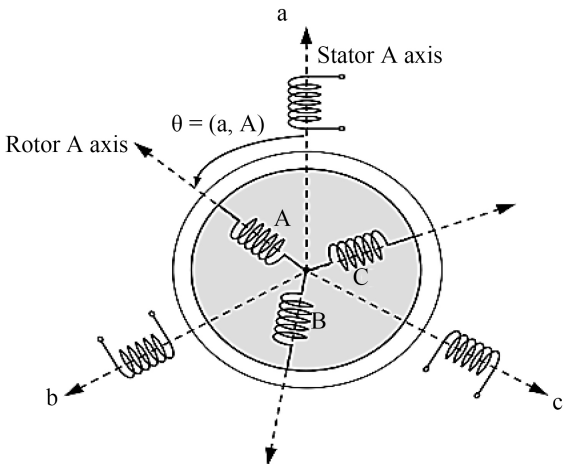

Figure 6. Schematic representation of the MAS.

3.4.2. Two-Phase Modeling of the Asynchronous Motor

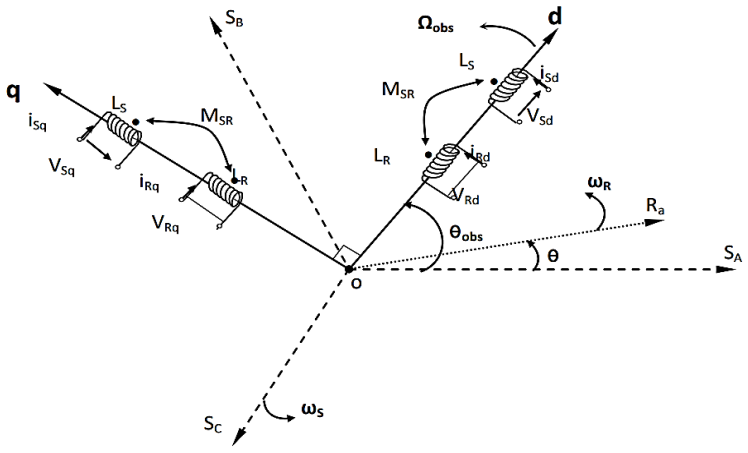

Figure 7. Park model of the MAS (three-phase to two-phase).

The transformation of the three-phase system into a two-phase system for the modeling of the synchronous machine (MAS) involves a change of reference that alters the physical quantities such as voltages, fluxes and currents [20]. This transformation results in equations independent of the angle θ and reduces the order of the machine equations. The Park transformation highlights the direct axis (d) in the Park frame, as well as the quadrature axis (q). **Figure 7** below shows the principle of the Park transformation [20] [21].

1) Tension equations

In a frame of reference linked to the rotating stator field, *i.e.* a frame of reference rotating at the stator pulsation speed $\omega = p.\ \Omega = d\text{ș}/dt$, the voltage equations in the Park frame are written [21]:

$$\begin{cases} Vsd = Rs*isd + \dfrac{d\varnothing sd}{dt} - \omega s\varnothing sq \\ Vsq = Rs*isq + \dfrac{d\varnothing sq}{dt} + \omega s\varnothing sd \end{cases}$$
$$\begin{cases} Vrd = Rr*ird + \dfrac{d\varnothing rd}{dt} - \omega r\varnothing rq = 0 \\ Vrq = Rr*irq + \dfrac{d\varnothing rq}{dt} + \omega r\varnothing rd = 0 \end{cases} \quad (10)$$

2) Flow equations

By performing the Park transformation on the equations relating to fluxes and currents, we can derive the electromagnetic relations of the machine [21].

$$\begin{cases} \varnothing sd = Ls*isd + Lm*ird \\ \varnothing sq = Ls*isq + Lm*irq \end{cases}$$
$$\begin{cases} \varnothing rd = Lr*ird + Lm*isd \\ \varnothing rq = Lr*irq + Lm*isq \end{cases} \quad (11)$$

3) Electromagnetic torque equations

It is necessary to enrich the electrical model by including the formulations of the electromagnetic torque as well as the speed, which allows to describe the mechanical behavior. The expression of the electromagnetic torque obtained is formulated as follows: [21]

$$Cem = p*M\left(isq.ird - isd.irq\right) = \frac{p.M}{Lr}\left(\varnothing rd.isq - \varnothing rq.isd\right) \quad (12)$$

4) Mechanical equations

$$j.\frac{d\Omega}{dt} + f.\Omega = Cem - Cr \quad (13)$$

So we can define the Park matrix as follows [6] [21]:

$$\left[P(\theta)\right] = \sqrt{\frac{2}{3}}\begin{bmatrix} \mathrm{Cos}\theta & \mathrm{Cos}\left(\theta - \frac{2\pi}{3}\right) & \mathrm{Cos}\left(\theta - \frac{4\pi}{3}\right) \\ -\mathrm{Sin}\theta & -\mathrm{Sin}\left(\theta - \frac{2\pi}{3}\right) & -\mathrm{Sin}\left(\theta - \frac{4\pi}{3}\right) \\ \frac{1}{\sqrt{2}} & \frac{1}{\sqrt{2}} & \frac{1}{\sqrt{2}} \end{bmatrix} \quad (14)$$

The inverse transformation of the Park Matrix exclaims:

$$\left[P(\theta)\right]^{-1} = \sqrt{\frac{2}{3}} \begin{bmatrix} \text{Cos}\theta & -\text{Sin}\theta & \frac{1}{\sqrt{2}} \\ \text{Cos}\left(\theta - \frac{2\pi}{3}\right) & -\text{Sin}\left(\theta - \frac{2\pi}{3}\right) & \frac{1}{\sqrt{2}} \\ \text{Cos}\left(\theta - \frac{4\pi}{3}\right) & -\text{Sin}(\theta - \frac{4\pi}{3} & \frac{1}{\sqrt{2}} \end{bmatrix} \quad (15)$$

3.4.3. Characterization of the Mill

The millet mill can be considered as a mechanical load for the engine. The model of the artisanal mill is defined by the load torque profile. The characteristic observed in the operation is that the grinding is done in steady state. The mechanical parameters (speed and torque) of the mill are a function of the flow and the grain (D). According to their operating principle, the speed varies with the flow rate, so there is a relationship between speed and flow rate [6] [22].

$$\omega = \omega s - k * D \quad (16)$$

With

$\boldsymbol{\omega}$: the rotation speed under load (rd/s);

$\boldsymbol{\omega s}$: the no-load rotation speed (rd/s);

K: the characteristic constant of the mill (rd/kg);

D: grain flow rate (Kg/s).

Using the fundamental operating concept of the artisanal mill as well as the interaction of the hammers (propellers) that reduce the grain size, it is possible to express the torque configuration as a fusion of the four pre-existing load couples. Equation (17) represents the formula of the mechanical characteristic as a function of the parameters (K, k1, k2, K3, K4) that define the specific properties of the mill [22]

$$Cr = k_1 + k_2\omega + k_3\omega^2 + k_4\omega^{-1} \quad (17)$$

With: Cr mill load torque (Nm);

K_1, K_2, K_3 K_4 and K: The characteristic constants of the Moulin.

The parameters of the mill used in this work are established by means of experimental tests. The corresponding values are presented in **Table 1** below [22].

Table 1. Mill parameter values.

Settings	Values
K_1 (Nm)	2091.5
K_2 (Nms/rd)	−12.031
K_3 (Nms^2/rd)	0.0171
K_4 (Nm Rd/s)	0
k (rd.kg)	5.8161
ωo (rd/s)	313.47

Then the resisting torque (Cr) becomes:

$$Cr = k_3\left(\omega_0 - k\,x\,D\right)^2 + k_2\left(\omega_0 - k\,x\,D\right) + k_1 \tag{18}$$

3.5. System Control

V/f scalar control with SVM (support vector machines) strategy is used for the control of the grinding device.

3.5.1. Scalar Command

The principle of scalar control is to keep the V/f ratio constant. Equation (19) gives the expression for the maximum torque [22].

$$C_{e\max} = \frac{3pL_m{}^2}{2L_s\left(L_sL_r - L_m\right)}\left(\frac{V_S - R_SI_S}{\omega_s}\right)^2 \tag{19}$$

The simplified expression, or the voltage drop across the stator resistance is neglected. However, at low speeds the voltage drop cannot be neglected. We propose to compensate the voltage drop by a threshold voltage (Vo) and to operate the motor at a standstill at a limit frequency (fo). **Figure 8** shows the profile of the voltage amplitude as a function of frequency [22] [23].

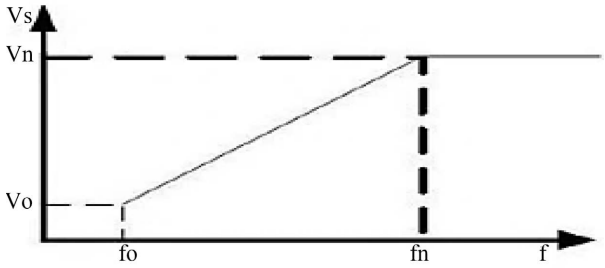

Figure 8. Modified V/f control profile.

The profile made it possible to establish the relation (20) giving the amplitude of the voltage (Vs) and the frequency (fo) from the nominal values of the voltage (Vn) and the frequency (fn) [23].

$$V_s = \frac{\left(V_n - V_0\right)}{\left(f_n - f_0\right)}\left(f_n - f\right) + V_0 \tag{20}$$

The closed-loop strategy is used to control the system. This strategy uses a loop that, from the mill speed error (ω), increases the frequency of the stator voltages to correct the speed error due to slip (ω_g). Equation (21) gives the generated stator pulsation (ω_s) [23].

$$\omega_s = \omega_g - \omega \tag{21}$$

The three voltages (i = 1, 2, 3), generated from the frequency, are given by equation (22).

$$V_i = \left(\frac{\left(V_n - V_0\right)}{\left(f_n - f_0\right)}\left(f_n - f\right) + V_0\right)\sin\left(2\pi ft - 2\frac{\left(i-1\right)}{3}\pi\right) \tag{22}$$

The generated voltages (Vi) and pulsations (ωs) are the input variables of the SVM (support vector machines) command.

3.5.2. Vector Control

The vector control technique is based on the orientation of the flux in the machine, at the stator, rotor or in the air gap, along one of the two axes (d) or (q) [24]. Therefore, the control of the currents along the d axis determines the magnetic state of the machine, while the control of the currents along the q axis provides us with the necessary torque [23] [24].

The equation that shows the relationship between the flux $\varnothing_r$ and the current i_{sd} is:

$$\begin{cases} C_{em} = k * i_{sq} \\ \dfrac{M}{T_r} i_{sd} = \dfrac{d\varnothing_r}{dt} + \dfrac{1}{T_r}\varnothing_r \end{cases} \tag{23}$$

It is observed that the direct stator current component i_{sd} determines the rotor flux amplitude, while the quadratic stator current component i_{sq} determines the torque.

1) Cruise control settings

The speed control chain can be schematically represented in (**Figure 9**) below [25]:

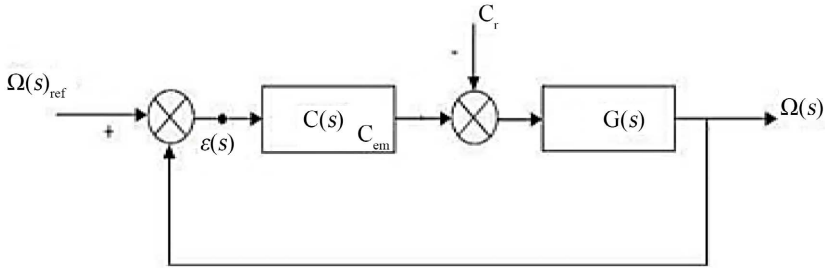

Figure 9. Speed control with a PI corrector.

$$\begin{cases} \dfrac{1}{\omega_n^{\,2}} = \dfrac{J}{K_i} & K_i = J.\omega_n^{\,2} \\ \dfrac{2\varepsilon}{\omega_n} = \dfrac{f + K_p}{K_i} & K_p = 2\varepsilon J\omega_n - f \end{cases} \tag{24}$$

$T_r\_w = 0.1$; % Response time at 5% of speed

$w_n\_T_r\_w = 3\%$ The settings for speed

$K_i\_w = wn^2 * J$

$K_p\_w = ((2*x_i * K_i\_w)/wn) - f_r$

2) Flow Regulator Settings

To ensure the proper operation of the machine, the total flux must be kept constant at its nominal value during speed variations or application of charge additives [24] [25].

The block diagram is given by (**Figure 10**):

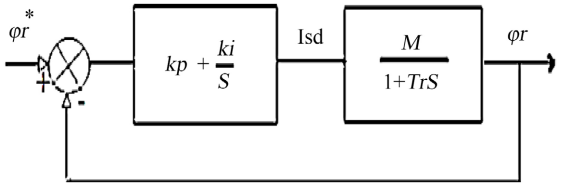

Figure 10. Flow control loop.

$$AG(s)=\frac{\frac{SK_{p+}K_i}{\tau_r}}{S^2.+S\left(\frac{L_mK_p+1}{\tau_r}\right)+\frac{L_mK_i}{\tau_r}} \tag{25}$$

For the control of the closed-loop system, it is necessary to carefully choose the coefficients K_i *et* K_p. The transfer function of a closed-loop system of order 2 is given by [16] [25].

$$\begin{cases} \frac{L_mK_p+1}{\tau_r}=2\rho & K_p=\frac{1}{L_m}\left(\frac{2L_r\rho}{R_r}-1\right) \\ \frac{L_mK_i}{\tau_r}=2\rho^2 & K_i=\frac{2L_r\rho^2}{R_r} \end{cases} \tag{26}$$

T_r_flux = 0.01; % Response time for the flow

% Parameters for the stream

K_i_phi = 1/(L_m * T_r_flux)

K_p_phi = (Lr/Rr) * K_i_phi

3.6. Simulation Results and Discussion

Scalar Command

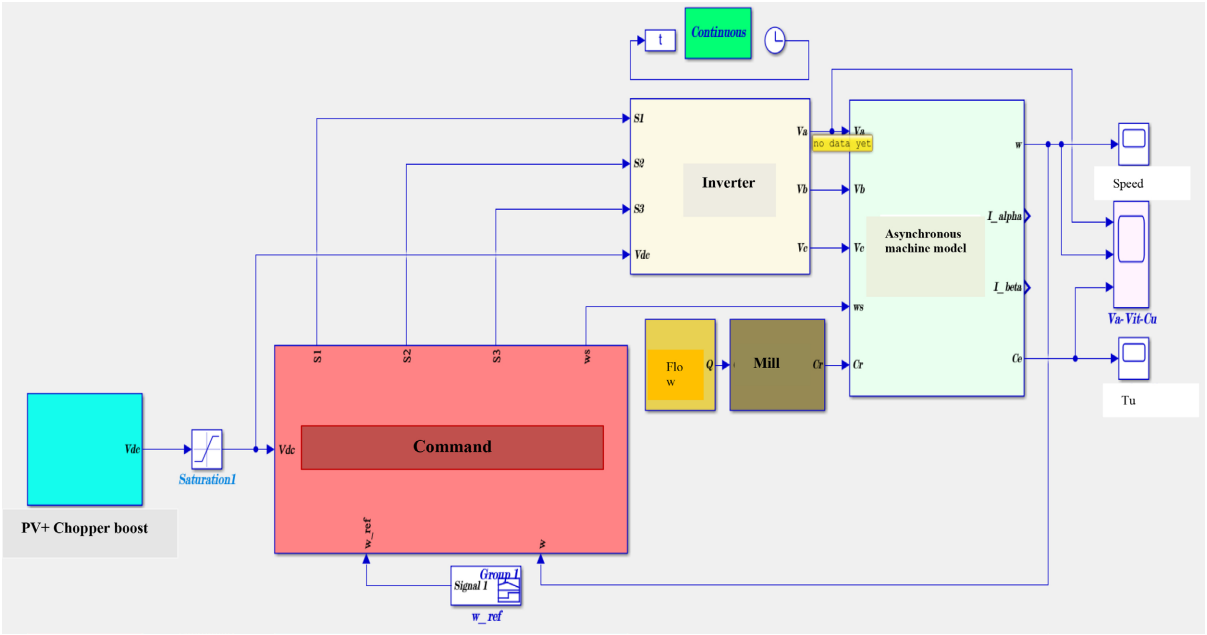

Figure 11. System model with scalar control on Matlab Simulink.

Figure 11 illustrates the configuration of the system integrating a solar panel (PV), a chopper, an inverter, a Solar Powered Motor (SPM) with its load (mill). This system is driven by a scalar control strategy [16].

The modeling and implementation of the scalar control strategy was carried out using Matlab/Simulink. This approach allowed to simulate the system, and the results were obtained by running the simulation of the model with the parameters that will be provided in the **Appendix**.

4. Discussion 1

During start-up, oscillations of the electromagnetic torque are observed due to the modulation (Transient) and harmonics carried by the inverter output signal during the start-up phase, then it decreases to an almost zero value from 0 to 3 s which corresponds to the no-load operation of the MAS, the electromagnetic torque therefore reaches a value and then follows its setpoint. It continues with less significant oscillations due to modulation around an average value corresponding to friction losses and ventilation. These oscillations then stabilize according to the value of the resistive torque Cr with a progressive and regressive application of the load (as illustrated in Figure 12).

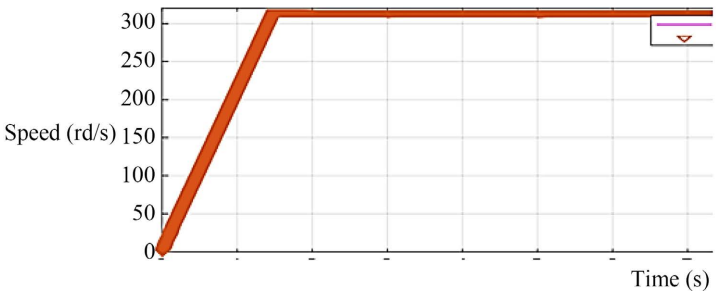

Figure 12. Mill speed characteristic.

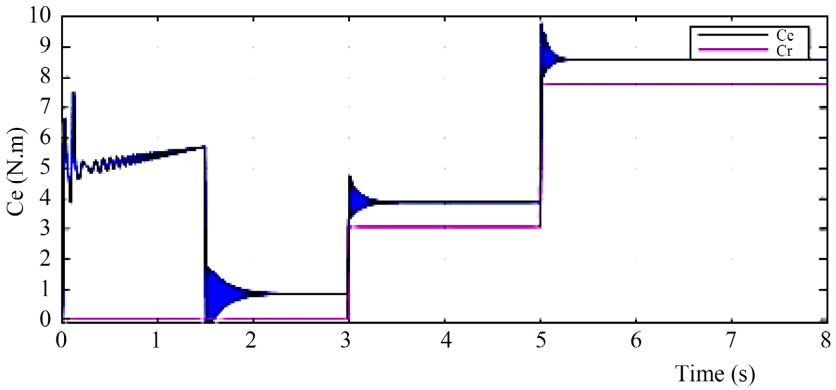

Figure 13. Characteristic of the variation of the resistive torque and the electromagnetic torque.

The simulation undertaken involves the application of a variable load profile that is representative of the resistive torque of the machine. For $\omega_{ref} = 314rd/s$

and a C_r variable applied at times t = 3 s, t = 5 s and t = 9 s we see that the electromechanical torque and the speed follow their reference value regardless of the value of the resistive torque applied (as illustrated in Figure 13).

The application of the variable load torque slightly reduces the rotation speed, which returns to its set value after a short time by the effect of the scalar control, hence a regulation perfectly ensured by the PI correctors

DFOC Vector Control

Figure 14 illustrates the configuration of the system integrating a solar panel (PV), a chopper, an inverter, a Solar Powered Motor (SPM) with its load (mill). This system is driven by a FOC (field oriented control) control strategy.

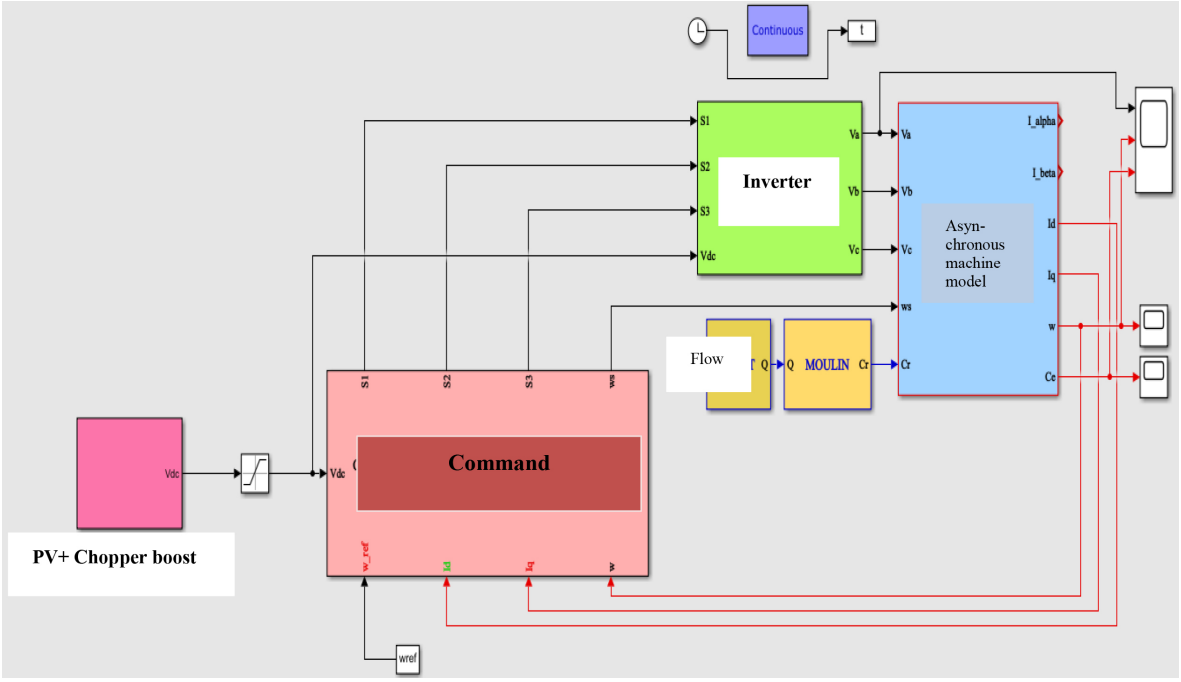

Figure 14. System model with vectorial control on Matlab Simulink.

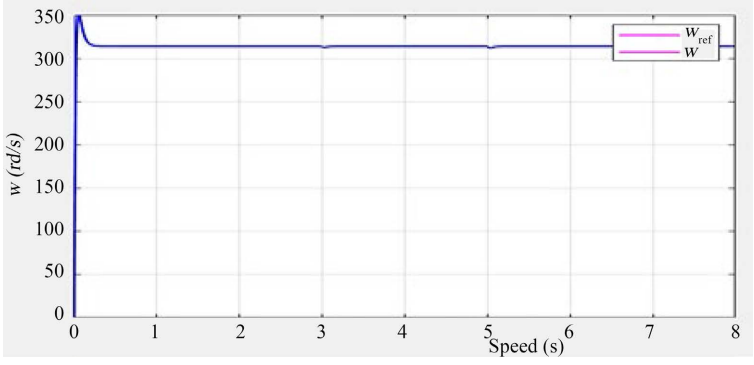

Figure 15. Mill speed characteristic.

The model creation and implementation of the FOC (Field Oriented Control)

control strategy were performed using Matlab/Simulink. This method was used to simulate the system and the results were obtained by running the model simulation.

Figure 16. Characteristic of the variation of the resistive torque and the electromagnetic torque.

5. Discussion 2

During startup, electromagnetic torque oscillations are observed due to modulation (Transient) and harmonics carried by the inverter output signal during the startup phase. It continues with less significant oscillations due to modulation around an average value corresponding to friction losses. These oscillations then stabilize from 0 to 3 s which corresponds to the no-load operation of the MAS and depending on the value of the resistive torque Cr with a progressive application of the load at time t = 5 s and at time t = 9 S corresponds to disturbances of variable load torque C_{rv} = 9.5 Nm and 6 Nm the torque undergoes a transaction peak when switching from one mode to another, then regains its value without error. This results in a gradual variation of the electromagnetic torque, in relation to the resistive torque.

The results obtained also demonstrate that, despite any variation in the load, the speed remains constant at 3000 rpm, which is equivalent to 325 rad/s as shown in (**Figure 15**). We also note that the system responds positively to this variation in the load, the speed perfectly follows its new reference with a small overshoot due to the PI regulator and it quickly reaches its setpoint during the start-up phase without the application of a load and during the progressive application at time t = 3 s and at time t = 5 s corresponds to disturbances of variable load torque C_{rv} = 0.4 Nm and 9.5 Nm and regressive load at time t = 9 s of C_{rv} 6 N, it undergoes a small attenuation which disappears thereafter to regain its imposed value with good dynamics . This means that the regulation is robust from the speed control point of view. Consequently, a regulation and a pursuit of the speed is set up in a completely effective manner.

The simulation undertaken involves the application of a variable load profile

that is representative of the machine's resistive torque (as illustrated in Figure 16).

Comparison of the Two Types of Orders

	Scalar	Vector
Rise time	248.673 ms = 0.248 s	19.254 ms = 0.019 s
Response time (Step Response)	829.8 ms = 0.8298 s	348 ms = 0.348 s
Overshoot	9.341%	11,798%
Peak to Peak	342	352

The rotation speed of the scalar control follows the reference in regulation and in pursuit with a rise time of 0.248 s and a response time of 0.8298 s after a transient regime observed at the time of start-up. The speed undergoes an overshoot of 9.341% for a time of 1.7 s then it returns to its setpoint and keeps this value in steady state until the load couples are applied, which it then regulates to return to the setpoint again.

The response of the vector control presents good results in pursuit (precision) of the setpoint and rejection of disturbances (Robustness) of load with an overshoot of 11.798%, a voltage peak of 352 V is observed then it quickly regains its setpoint with a rise time of 0.0119 s showing the speed of the system and a response time of 0.348 s.

To regulate the mill speed, we used both control methods: scalar control and vector control, which provide precise control and improve energy efficiency. A comparative study between the two methods shows that scalar control (Discussion 1), simpler and less expensive, is advantageous for a small-scale mill powered by an asynchronous motor and a photovoltaic system. Although vector control offers better performance (Discussion 2), its complexity and higher cost are not justified for rural applications where scalar control effectively meets the needs. After analysis, we chose scalar control as the optimal solution.

6. Conclusion

This paper explores scalar and vector control approaches to maintain a constant mill speed, despite variations in solar irradiance and load. Matlab-Simulink simulations confirm these results. The choice of scalar control, based on economic and feasibility analysis, allows us to adjust the mill speed precisely, thus optimizing the quality of the final product (4800 rpm for flour, 3000 rpm for broken cereals). Despite the progress made, future research could explore adaptive control methods and the integration of machine learning to improve speed regulation and system efficiency.

Conflicts of Interest

The authors declare no conflicts of interest regarding the publication of this paper.

References

[1] Aouchiche, N., Aït Cheikh, M.S. and Malek, A. (2021) Tracking the Maximum Power Point of a Photovoltaic System by the Methods of Conductance Incrementation and Perturbation & Observation. *Renewable Energy Review*, **16**, 485-498.

[2] Doumbia, M.L. and Traoré, A. (2000) Modelling and Simulation of an Asynchronous Cage Machine Using Matlab/Simulink Software. https://ro.scribd.com/document/502417279/01-9

[3] Robyns, B., Francois, B., Degobert, P. and Hautier J.P. (2018) Vector Control of Induction Machines. Springer. https://doi.org/10.1007/978-0-85729-901-7

[4] Fatima, M. and Assia, H. (2024) Performances of an Asynchronous Motor Powered by a Photovoltaic Generator. *Journal of Electrical Systems*, **20**, 2899-2908. https://journal.esrgroups.org/jes/article/view/7971

[5] Yahya, A.O.M., Ould Mahmoud, A. and Youm, I. (2020) Study and Modeling of a Photovoltaic Generator. *Renewable Energy Review*, **11**, 473-483.

[6] Diop, M., Thiaw, L., Thiam, M., Mbodji, M. and Diaw, N. (2016) Efficient Control of a Three Induction Motor Driving a Craft Mill of Millet. *International Journal of Scientific & Technology Research*, **5**, 88-91.

[7] Ouali, A. and Tahri, M. (2018) Scalar Control of an Asynchronous Motor. https://dspace.ummto.dz/items/49a2d1ca-f111-4abe-803b-6771d287abff

[8] Essakhi, H. and Farhat, S. (2019) Modeling and Simulation of a Photovoltaic Module. 5*th International Materials and Environment Days* (*JIME* 2019). https://www.researchgate.net/publication/332846895

[9] Diop, M., Ba, O., Niang, B., Ngom, I. and Thiaw, L. (2020) A Methodology for Modeling Cereal Milling System. 2020 *International Conference on Electrical*, *Communication*, *and Computer Engineering* (*ICECCE*), Istanbul, 12-13 June 2020, 1-5. https://doi.org/10.1109/icecce49384.2020.9179182

[10] Xu, D., Wang, B., Zhang, G., Wang, G. and Yu, Y. (2018) A Review of Sensorless Control Methods for AC Motor Drives. *CES Transactions on Electrical Machines and Systems*, **2**, 104-115. https://doi.org/10.23919/tems.2018.8326456

[11] Kurani, A., Doshi, P., Vakharia, A. and Shah, M. (2021) A Comprehensive Comparative Study of Artificial Neural Network (ANN) and Support Vector Machines (SVM) on Stock Forecasting. *Annals of Data Science*, **10**, 183-208. https://doi.org/10.1007/s40745-021-00344-x

[12] Sathishkumar, H. (2019) Performance Analysis of Speed Controller for 3hp and 150hp Three Phase Induction Motors Being Used in Cable Industry Applications. *Asian Journal of Electrical Sciences*, **8**, 7-14. https://doi.org/10.51983/ajes-2019.8.1.2339

[13] Akkouchi, K., Rahmani, L. and Lebied, R. (2021) New Application of Artificial Neural Network-Based Direct Power Control for Permanent Magnet Synchronous Generator. *Electrical Engineering & Electromechanics*, **6**, 18-24. https://doi.org/10.20998/2074-272x.2021.6.03

[14] Ali, A.J., Farej, Z. and Sultan, N. (2019) Performance Evaluation of a Hybrid Fuzzy Logic Controller Based on Genetic Algorithm for Three Phase Induction Motor Drive. *International Journal of Power Electronics and Drive Systems* (*IJPEDS*), **10**, 117-127. https://doi.org/10.11591/ijpeds.v10.i1.pp117-127

[15] Latif, S., Zou, Z., Idrees, Z. and Ahmad, J. (2020) A Novel Attack Detection Scheme for the Industrial Internet of Things Using a Lightweight Random Neural Network. *IEEE Access*, **8**, 89337-89350. https://doi.org/10.1109/access.2020.2994079

[16] Dybkowski, M. and Klimkowski, K. (2019) Artificial Neural Network Application for Current Sensors Fault Detection in the Vector Controlled Induction Motor Drive. *Sensors*, **19**, Article 571. https://doi.org/10.3390/s19030571

[17] Alhajeri, M.S., Luo, J., Wu, Z., Albalawi, F. and Christofides, P.D. (2022) Process Structure-Based Recurrent Neural Network Modeling for Predictive Control: A Comparative Study. *Chemical Engineering Research and Design*, **179**, 77-89. https://doi.org/10.1016/j.cherd.2021.12.046

[18] Mesai-Ahmed, H., Bentaallah, A., Cardoso, A.J.M., Djeriri, Y. and Jlassi, I. (2021) Robust Neural Control of the Dual Star Induction Generator Used in a Grid-Connected Wind Energy Conversion System. *Mathematical Modelling of Engineering Problems*, **8**, 323-332. https://doi.org/10.18280/mmep.080301

[19] Zeb, K., Uddin, W., Haider, A., Belal, S., Mehmood, C.A., Khan, M.A., et al. (2017) Robust Speed Regulation of Indirect Vector Control Induction Motor Using Fuzzy Logic Controllers Based on Optimization Algorithms. *Electrical Engineering*, **100**, 787-802. https://doi.org/10.1007/s00202-017-0553-z

[20] Bana, P.R. and Amin, M. (2021) Adaptive Vector Control of Grid-Tied VSC Using Multilayer Perceptron-Recurrent Neural Network. *IECON* 2021—47*th Annual Conference of the IEEE Industrial Electronics Society*, Toronto, 13-16 October 2021, 1-6. https://doi.org/10.1109/iecon48115.2021.9589975

[21] Benayad, N. and Tria, T.E. (2020) Application of Advanced Techniques for the Control of an Asynchronous Machine. University Echahid Cheikh Larbi Tebessi. http://oldspace.univ-tebessa.dz:8080/xmlui/handle/123456789/7266

[22] Venu Gopal, B.T. and Shivakumar, E.G. (2018) Design and Simulation of Neuro-Fuzzy Controller for Indirect Vector-Controlled Induction Motor Drive. In: Nagabhushan, P., Guru, D., Shekar, B. and Kumar, Y., Eds., *Data Analytics and Learning*, Springer, 155-167. https://doi.org/10.1007/978-981-13-2514-4_14

[23] Gupta, H., Varshney, H., Sharma, T.K., Pachauri, N. and Verma, O.P. (2021) Comparative Performance Analysis of Quantum Machine Learning with Deep Learning for Diabetes Prediction. *Complex & Intelligent Systems*, **8**, 3073-3087. https://doi.org/10.1007/s40747-021-00398-7

[24] Hannan, M.A., Ali, J.A., Ker, P.J., Mohamed, A., Lipu, M.S.H. and Hussain, A. (2018) Switching Techniques and Intelligent Controllers for Induction Motor Drive: Issues and Recommendations. *IEEE Access*, **6**, 47489-47510. https://doi.org/10.1109/access.2018.2867214

[25] Khoei, H.R. and Zolfaghari, M. (2016) New Model Reference Adaptive System Speed Observer for Field-Oriented Control Induction Motor Drives Using Neural Networks. *Bulletin of Electrical Engineering and Informatics*, **5**, 25-36. https://doi.org/10.11591/eei.v5i1.520

Appendix

```
clear all
clc
%% Mini-grid settings
f = 50; % network frequency
Ve = 230; % Network voltage
Rrr = 0. 808; % The internal resistance of the mini-grid
Lrr = 3e−3; % The internal inductance of the network
%% Output and command parameters %%
Vsref = 565;
reference voltage
Ps = 4000; % Output power
Rch = Vsref^2/Ps; % Output resistance
Is = Ps/Vsref; % Output current
Vp = 1;
Go = Vsref/Vp;
Fc = 10e 3; % Switching Frequency
Di = 1; %The current ripple
Dv = 1.5; % Voltage ripple
Lsr = Vsref/(2*Di*Fc ); % leakage inductance
C = (Ps/Vsref)/(2*3.14*Dv*f); %Capacity
wc_i = 2500;
wc_v = 10;
Tau_i =(Lsr + Lrr)/Rrr
Goi = Go/Rrr
Gov = (Rch*Ve* sqrt (2))/(4*Vsref)
Tau_v = (Rch*C)/2
% kpv = (1.14*Tau_v*wc_v − 1)/(Gov)
% kiv = (Tau_v*wc_v^2)/(Gov)
% kpi = (1.14*Tau_i*wc_i−1)/(Goi)
% kii = (Tau_i*wc_i^2)/(Goi)
TrepI = 0.001
TrepV = 0.07
kpv = (Tau_v/Gov)*(1/TrepV)
kiv = (1/Gov)*(1/TrepV)
kpi = (1/Goi)*(Tau_i/TrepI)
kii = (1/Goi)*(1/TrepI)
% MACHINE PARAMETERS
Rs = 2.475; % Stator resistance
Rr = 4.446; % Rotor resistance
Ls = 270.315e−3; % Stator inductance
Lr = 270.315e−3; % Rotor inductance
Lm = 259.836e−3; % Mutual inductance
```

```
= 1; % Number of Pole Pairs
J = 0.023; % Moment of inertia
fr = 26e−4; % Coefficient of friction
% THE CONSTANTS
Sigma = 1 − ((Lm*Lm)/(Lr*Ls));
Lss = Ls*sigma;
Tr = Lr/Rr;
%REFERENCES
Ts = 10e−4; % SVM switching period
Phi_n = 1; % Nominal flow
wref = 314; % Reference Speed
Vdc = 565; % DC bus voltage
% SYNTHESIS OF CORRECTORS FOR THE FOC
%The coefficients
wn = wn_Tr_w/Tr_w; % Clean pulsation
Tr_i = 0.00001; % Current response time
wnTrep = 3;
%Parameters for currents
Ki_i = Rs/Tr_i;
Kp_i = Lss/Tr_i;
```